INTERNATIONAL JOURNAL FOR NUMERICAL METHODS IN FLUIDS
Int. J. Numer. Meth. Fluids 2005; **48**:1219–1240
Published online 13 April 2005 in Wiley InterScience (www.interscience.wiley.com). DOI: 10.1002/fld.972

A nonlinear atomization model for computation of drop size distributions and spray simulations

Hongbok Park[1,‡], Sam S. Yoon[2,§] and Stephen D. Heister[1,*,†]

[1]*School of Aeronautics and Astronautics, Purdue University, W. Lafayette, IN 47907 – 2023, U.S.A.*
[2]*Sandia National Laboratories, Fire Science & Technology Department, P.O. Box 5800, Albuquerque, NM 87185-1135, U.S.A.*

SUMMARY

A model has been developed to provide a comprehensive simulation of a spray formed by a high-speed liquid jet. The primary atomization process is simulated in a completely nonlinear fashion using the boundary element method under the assumption of axisymmetric, inviscid flow. The presence of the orifice boundary layer is simulated with a ring vortex whose strength and location are uniquely determined from boundary layer properties at the orifice exit plane. Droplet and axisymmetric ligament tracking models have been developed to provide more comprehensive spray simulations. The breakup of the axisymmetric ligaments shed from the parent surface is assessed both in a nonlinear fashion as well as using the linear stability analysis of Ponstein. Using this latter approach, drop size distributions have been generated from first principles and compared with the popular Rosin–Rammler model. Copyright © 2005 John Wiley & Sons, Ltd.

KEY WORDS: liquid jet; spray; atomization; drop size

1. INTRODUCTION

The hydrodynamic instability of liquid jets has been of great interest to fluid dynamicists for more than 100 years. Numerous linear theories have had some recognizable success in predicting the most unstable wavelength although these theories often give tenuous results in predicting droplet sizes. While the theories work well for modest deformations, nonlinear

*Correspondence to: Stephen D. Heister, School of Aeronautics and Astronautics, Purdue University, W. Lafayette, IN 47907 – 2023, U.S.A.
†E-mail: heister@ecn.purdue.edu
‡E-mail: hbpark@purdue.edu
§E-mail: ssyoon@sandia.gov

Contract/grant sponsor: Airforce Office of Scientific Research; contract/grant number: F49620-03-1-0025
Contract/grant sponsor: Sandia National Laboratories; contract/grant number: DE-AC04-94AL85000

Received 28 February 2005
Revised 21 July 2005
Accepted 2 March 2005

effects lead to errors in predicted droplet sizes even for low-speed laminar jets. Theories for obtaining an accurate prediction for the high-speed turbulent jet are even more severely lacking as the complexity of the flow field and the number of droplets formed increases dramatically. The behaviour of a high-speed jet is influenced by many instability sources such as boundary layer instability within the pipe flow [1–9], cavitation disturbances emanating from the sharp corners inside the orifice passage [10–14], turbulence [15–19], and the shear layer-driven instability between the exited liquid flow and the surrounding gas [20–22]. At present, most analytical models are linear and are based on the Kelvin–Helmholtz instability between liquid and gas. Accounting for the other factors in an analysis typically requires a nonlinear treatment.

Recent efforts [8], primarily focused on the boundary layer instability mechanism, have shown that this mechanism plays a prominent role for high-speed laminar and turbulent jets. The boundary layer instability exists in all jets due to Rayleigh's theorem; 'Velocity profiles with *points of inflection* are unstable'. Rayleigh proved that the presence of a point of inflection is a *necessary* (though it is not *sufficient*) condition for the appearance of unstable waves. These unstable waves eventually appear on the liquid surface for all liquid jets when the boundary layer instabilities are not obscured by other instability mechanisms. Further detailed description is available by Yoon and Heister [23].

The model developed by Yoon and Heister [8] provides the point of departure for the present studies. This nonlinear, axisymmetric boundary element model was utilized to simulate boundary layer instability mechanisms with favourable comparisons against the measurements in Hoyt and Taylor's [9] experiments. The model presumes that the annular ligaments pinched from the jet periphery undergo secondary atomization due to azimuthal instabilities. The linear stability analysis due to Ponstein [24] is then used to predict the size of droplets formed from each ligament. Yoon and Heister [8] did not address the spray evolution and subsequent droplet size statistics borne out of a given orifice design and flow condition. Moreover, the model presumed that annular ligaments shed from the periphery of the jet were inherently stable such that further atomization of these structures were attributed to circumferential modes leading to the ultimate droplet/spray formation.

The present studies focus on improvements to the existing capability. Numerical improvements are implemented to permit solution of larger problems such that formation of a complete liquid core is now possible for some flow conditions. Droplet tracking algorithms have been developed to permit simulation of quasi-three-dimensional sprays. A complete spray evolution is presented using these enhanced capabilities. Finally, individual annular ligaments have been tracked in order to assess their overall stability and subsequent influence on droplet statistics. Theoretical droplet distributions are compared to classical empirical models [25].

2. MODEL DESCRIPTION

2.1. Governing equation

Reference [8] provides a complete description of the model elements; in the interest of brevity, only highlights will be presented here. The formulation of the boundary element method (BEM) starts with the integral representation of Laplace's equation, $\nabla^2\phi = 0$, with ϕ being the velocity potential under the assumption that the liquid is inviscid and incompressible.

Following Liggett and Liu [26], the integral equation for this Laplace's equation is:

$$\alpha\phi(\mathbf{r}_i) + \int_S \left[\phi \frac{\partial G}{\partial \hat{n}} - qG \right] \mathrm{d}s = 0 \tag{1}$$

where $\phi(\mathbf{r}_i)$ is the value of the potential at a point $\mathbf{r}_i$, S is the boundary of the 2-D domain, α is the singularity contribution of boundary point, and G is the free space Green's function corresponding to Laplace's equation. Linear elements are assumed in discretization of the velocity potential, and its normal velocity, $q = \partial\phi/\partial n$. Jet velocity ($U$), the orifice radius ($a$), and the liquid density (ρ_l) are used as the non-dimensional parameters. The unsteady Bernoulli equation is used as a boundary condition along a free surface interface as follows:

$$\frac{\partial \phi}{\partial t} + \frac{1}{2}|\nabla \phi_\mathrm{t}|^2 + P_\mathrm{g} + \frac{\kappa}{We} - \frac{Bo}{We} z = 0 \tag{2}$$

where $()_\mathrm{t}$ represents the total value for ϕ, P_g is the gas pressure, κ is the curvature of the free surface, and the Weber number and Bond number are defined as

$$We = \frac{\rho_\mathrm{l} U^2 a}{\sigma}, \quad Bo = \frac{\rho_\mathrm{l} g a^2}{\sigma} \tag{3}$$

A more general solution can be obtained through the principle of superposition for potential flow. A potential ring vortex is placed near the orifice exit plane to simulate the presence of the internal boundary layer. The circulation strength, Γ_v, and location of the potential ring vortex are uniquely determined by the bulk orifice flow and the boundary layer thickness at the orifice exit plane [8]. Figure 1 depicts the typical computational domain indicating the location of the ring vortex, the mesh spacing Δs, and parameters used to set the local mesh spacing, R_c and z_l. Since the Laplacian governing equation is linear, we may superimpose the main potential flow with the potential vortex ring:

$$\phi_\mathrm{t} = \phi + \phi_\mathrm{v} \tag{4}$$

Since the differential operator is a linear function, the superposition theory holds for the velocity as well:

$$u_\mathrm{t} = u + u_\mathrm{v}, \quad v_\mathrm{t} = v + v_\mathrm{v} \tag{5}$$

where $u = \partial\phi/\partial z$ and $v = \partial\phi/\partial r$ and u_v, v_v are axial and radial velocities induced by the presence of the vortex ring. Applying the Reynolds transport theorem to Equation (2) and combining the theory of superposition gives the following nonlinear boundary condition for the free surface:

$$\frac{\mathrm{D}\phi}{\mathrm{D}t} = \frac{1}{2}|\mathbf{u}_\mathrm{t}|^2 - \mathbf{u}_\mathrm{t} \cdot \mathbf{u}_\mathrm{v} - P_\mathrm{g} - \frac{\kappa}{We} + \frac{Bo}{We} z \tag{6}$$

Equation (4) provides a relation for the time rate of change of ϕ subject to the influence of dynamic pressure changes, pressure imposed from a gas phase (if present), surface tension, and gravitational hydrostatic forces. In the present work, the gas phase and gravity have been neglected such that P_g and Bo are assumed to be zero. Analytical solutions for the vortex-ring-induced velocities, are a function solely of the vortex strength and nodal locations and are derived and summarized in Reference [27].

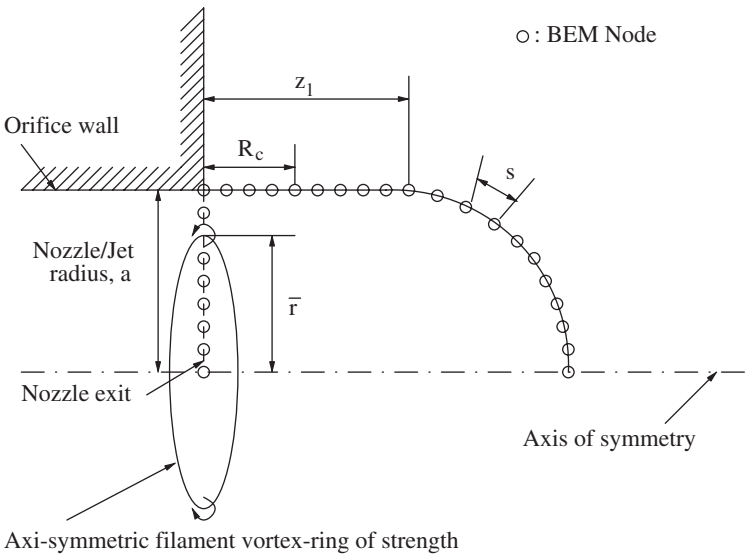

Figure 1. Model schematic.

For all simulations, the strength of the imposed vorticity, which imposes vortical velocities shown in Equation (5), is based on circulation across the laminar boundary layer. The most dominant wavelength caused by boundary layer instability is used for approximating the circulation of the vortex ring at the nozzle exit [28]. Thus,

$$\Gamma_v = U\lambda \tag{7}$$

The boundary layer wave is approximated using the Brennen [28] theory, $\lambda = (2\pi/\gamma)\delta_2$, where $\gamma = 0.175$, and δ_2 is the momentum thickness of the laminar flow [29]. Detailed information on the vortex ring strength is found in References [8, 30].

2.2. *Droplet tracking*

The spray evolution was not provided in the original BEM calculation [8] since the simulation was only conducted on the jet core. However the actual spray is formed by the jet core and the cone angle formed by the velocity of shed droplets. If the droplet movement after pinch-off can be tracked, it will enhance understanding of the flow characteristics of the spray. In addition, it could give more information including the aerodynamic effects on droplet dynamics with the dispersion angle. Since the droplets experience aerodynamic drag while traveling in gas, the velocity could be slightly different according to the measured location. The original model predicts the longitudinal velocity and the Sauter mean diameter (SMD) very well for Hoyt–Taylor's jet [9] of $U = 21$ m/s. While the axial velocity is in good agreement with Wu *et al.*'s observation [16] as $u_D = 0.76U$, the lateral velocity does not agree with the experimental data as $v_D = 0.42U$ while it was $0.07U$ in the experiment [16]. Here, the experimental data is measured at some distance from the jet core, the BEM result gives the value on the

jet surface just after pinch-off. Wu *et al.*'s data was recorded at a few nozzle diameters away from the centreline (i.e. $r/d \sim 2$ or 3).

The droplet diameter after pinch-off is calculated from the linear theory due to Ponstein [24] and the initial condition (i.e. initial velocity and position of each droplet) is then known as the result of the BEM simulation assuming that droplets are instantaneously pinched from the axisymmetric ring-shaped ligaments formed from the liquid core. The equivalent circular diameter of the ring-shaped ligaments is used with Ponstein's analysis that provides most unstable azimuthal wavelengths for a circular ring with circulation [8]. The output from this computation is then used as the input of the droplet tracking programme. Newton's second law is applied to describe the motion of a droplet assuming aerodynamic drag to be the only external force acting on a droplet.

$$m_{\mathrm{D}} \frac{\mathrm{d}\vec{u}_{\mathrm{D}}}{\mathrm{d}t} = C_{\mathrm{D}} \frac{1}{2} \rho_{\mathrm{g}} (\mathbf{u}_{\mathrm{g}} - \mathbf{u}_{\mathrm{D}}) |\mathbf{u}_{\mathrm{g}} - \mathbf{u}_{\mathrm{D}}| A_{\mathrm{D}} \tag{8}$$

where A_{D} is the projected area of a droplet ($\pi D^2/4$), m_{D} and $\mathbf{u}_{\mathrm{D}}$ are droplet mass and velocity, respectively. $\mathbf{u}_{\mathrm{g}}$ is an air velocity whose value is zero while assumed stationary air. C_{D} is the drag coefficient for the solid sphere given by Hwang *et al.* [31] below:

$$C_{\mathrm{D}} = \begin{cases} \dfrac{24}{Re_{\mathrm{D}}} \left(1 + \dfrac{1}{6} Re_{\mathrm{D}}^{1/3} \right), & Re_{\mathrm{D}} \leqslant 1000 \\ 0.424, & Re_{\mathrm{D}} > 1000 \end{cases} \tag{9}$$

where $Re_{\mathrm{D}} = UD/v_{\mathrm{air}}$.

Equation (5) is a second-order ODE for position and it is formulated as a system of first-order ODEs prior to integration. The system of equations can be written by using state variables as

$$\begin{aligned} \mathbf{y}_1 &= \mathbf{u}_{\mathrm{D}} \\ \mathbf{y}_2 &= \mathbf{y}_1' = \frac{\mathrm{d}\mathbf{u}_{\mathrm{D}}}{\mathrm{d}t} = C_{\mathrm{D}} \frac{1}{2} \rho_{\mathrm{g}} |\mathbf{y}_1|^2 A_{\mathrm{D}} / m_{\mathrm{D}} \end{aligned} \tag{10}$$

The fourth-order Runge–Kutta time marching scheme is used to solve this system of ODEs. The initial condition of each droplet is set by the pinch-off condition which is a result of the BEM calculation. Vaporization and collisions between droplets (and potential bouncing, atomization, and coalescence outcomes) are neglected for this simulation. Both 2-D and 3-D droplet tracking algorithms have been developed to simulate droplet trajectories subsequent to ring formation.

Since many thousands of droplets have to be tracked simultaneously, the routine was optimized as much as possible. To do this, the simulation for every droplet, which exists within an integration interval, is done simultaneously at each time step. Here the integration, dt, is set as a variable by the time interval to next droplet formation time. As a result, the program takes approximately 6 h for full 3-D tracking of thousands of droplets on a PC having a Athalon 1.0 GHz CPU.

2.3. Secondary breakup of ligament

The current spray jet simulation based on a BEM method shows good agreement [8] with the Wu and Faeth's experiment [17] and the predicted results by Brennen's linear theory [28]. However, it shows significant differences at higher jet velocities. The possible axisymmetric instability of the ring-shaped ligaments could potentially account for some of the differences as Ponstein's analysis really only addresses circumferential modes. If ligaments shed from the parent jet could be tracked in order to assess the potential for secondary breakup in the axisymmetric modes, it would be helpful in explaining the differences. Thus, the code was improved in order to simulate the secondary instability for each ring-shaped ligament after pinch-off events. Here, the value of ϕ at the pinch-off instant will be used as the initial condition for the subsequent surface evolution integration. The non-dimensional parameters remain identical to the parent jet, but the reference length and velocity is changed to the average ligament radius and average velocity to facilitate graphical depiction of the results.

The non-dimensional form of the unsteady Bernoulli equation is shown in Equation (2) assuming the jet velocity (U), the orifice radius (a), and the liquid density (ρ_l) serve as the basis for the non-dimensionalization. Here we need to change these parameters to the characteristic values of the pinch-off ligament; i.e. the pinch-off ring velocity (U_r) and ring radius (a_r) instead of parent jet's properties, which is given from the result of parent jet simulation.

Then the non-dimensional governing equation is obtained as follows:

$$\frac{\partial \phi_r}{\partial t_r} + \frac{1}{2}|\nabla \phi_r|^2 + P_g + \frac{\kappa_r}{We_r} - \frac{Bo_r}{We_r} z_r = 0 \tag{11}$$

with the non-dimensional parameters having the property of pinch-off ring as shown:

$$\nabla \phi_r^* = \frac{\nabla \phi_r}{U_r}, \quad \phi_r^* = \frac{\phi_r}{U_r a_r}, \quad P_g^* = \frac{P_g}{\rho_l U_r^2}, \quad t_r^* = \frac{U_r}{a_r} t_r \tag{12}$$

The new Weber number is given as

$$We_r = \frac{\rho_l U_r^2 a_r}{\sigma} \tag{13}$$

Basically, the non-dimensional form is not changed regardless of what is chosen as the reference. However we need to get the transfer factor between these two different presentations because the simulation result of jet core will be used as the input for initial condition of pinch-off ring. Matching Equations (3) and (12) at the just pinching event gives:

$$\phi^* = U_r a_r \phi_r = U_j a_j \phi_j \;\Rightarrow\; \phi_r = \frac{U_j a_j}{U_r a_r} \phi_j \tag{14}$$

where subscript j denotes the parent jet.

Also z and r should be changed by the same rate of reference length variation as

$$z^* = a_r z_r = a_j z_j \;\Rightarrow\; z_r = a_j / a_r \cdot z_j \tag{15}$$

$$r^* = a_r r_r = a_j r_j \;\Rightarrow\; r_r = a_j / a_r \cdot r_j \tag{16}$$

Using Equations (14)–(16), the transfer factors for our simulation of the Hoyt–Taylor [9] jet are obtained as follows:

$$\begin{aligned} \phi_r &= 11.54\ \phi_j, \qquad We = 1503.0 \\ z_r &= 10.5\ z_j, \qquad r_r = 10.5\ r_j \end{aligned} \tag{17}$$

with jet radius $(a_j) = 3.2$mm, average ring radius $(a_r) = 1/10.5 a_j$, and jet velocity $(U_j) = 21$m/s, and average ring velocity $(U_r) = 0.910 U_j$.

When the current axisymmetric BEM code can be expanded to simulate the behaviour of separated ligament from the parent jet, the BEM integration part for the governing equation does not require any modification. However, the current code was slightly modified because the boundary condition is different from that of jet simulation. A successive over-relaxation (SOR) method has been employed as an iterative approach to inverting the linear matrices formed from the discretization process. This approach has permitted solution of larger problems than those which were practical using the LU decomposition scheme described in prior work [8].

2.4. *Effect of smoothing frequency*

The surface shape of higher speed jets is so complex that it makes it very difficult to predict the surface properties such as curvature and gradient, which are crucial in the BEM scheme. Moreover, due to limited computer resources, we have been limited to the use of moderate-sized grids. For this reason, numerical smoothing is needed for getting the local gradient, curvature, and so on. That is, the smoothing frequency influences the final status

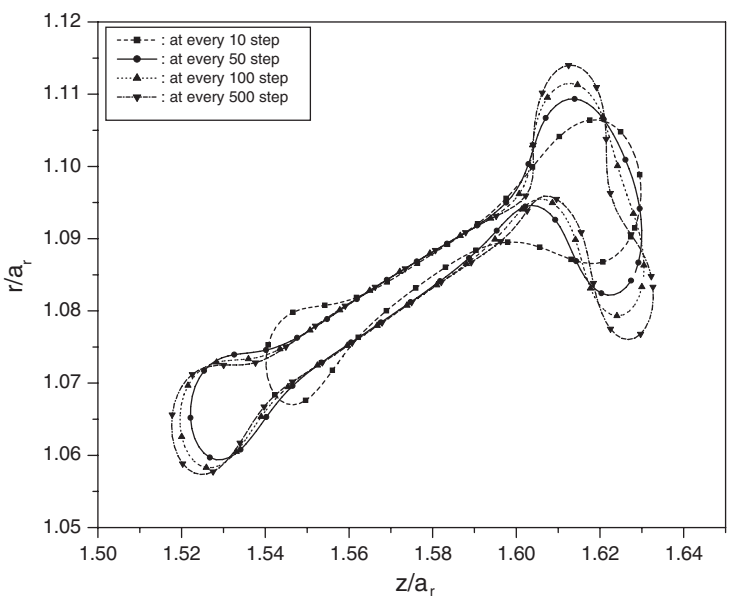

Figure 2. Ligament shape comparison according to the smoothing frequency at $t^* = 3.0$. This is the 94th ligament of Hoyt–Taylor jet, a typical ligament shape encountered in the simulation.

but it is needed for longer simulations. While this numerical smoothing suppresses propagation of local error to whole regions, it can give a deformed solution with excessive loss of surface characteristics. Thus, minimizing the smoothing frequency is desired but the numerical smoothing cannot be avoided for higher speed jet simulations [32]. The smoothing has been performed at every step about ϕ and the velocity normal to the local surface, q, for simulations conducted herein.

Since the ligaments shed from the parent jet have smaller velocities and diameters, which lead to a smaller Weber number, the surface deformation is much smaller. That is, because the local surface shape deformation is relatively small, we can lessen the smoothing frequency considerably to get the surface properties. Compared with the whole jet structure, the ligament size is very small. For this reason, this ligament is composed several grid points. Additional nodes are therefore inserted using cubic-spline interpolation to enhance resolution for ligament tracking purposes.

The shape evolution is changed according the smoothing frequency and excessive smoothing leads loss of the surface characteristics. However, less smoothing could make the code fail for ligament simulations having more complicated surface shapes. The 5 point explicit filter was once per every 50 steps; results for different smoothing frequencies are shown in Figure 2.

3. RESULTS AND DISCUSSION

Ponstein's [24] linear stability theory of a vortex ring assuming an instantaneous breakup is applied to obtain the droplet diameter after pinch-off. The free surface is unstable due to the vorticity present at the nozzle exit. During transitional flow, the axisymmetrically disturbed wave forms a 'finger-like' ligament and breaks up into several segments. Ponstein provided the dispersion equation of the vortex ring as

$$w^2 = \left[\frac{\sigma}{\rho a_r^3} (1 - k^2 a_r^2) + \left(\frac{\Gamma_r}{2\pi a_r^2} \right)^2 \right] (k a_r) \frac{I_1(k a_r)}{I_o(k a_r)} \tag{18}$$

where w is the growth rate, and a_r and Γ_r are the radius and the circulation of the vortex ring, respectively.

The use of Ponstein's analysis provides a powerful tool to extend an axisymmetric simulation to provide quasi-three-dimensional representations of sprays formed from high-speed jets. The technique provides a practical treatment given the fact that current computational resources limit the fully 3-D simulation and tracking of sprays. However, the 3-D instability is known to manifest itself prior to pinching of annular ligaments as noted in the classic Hoyt and Taylor work as well as in more recent work of Marmottant and Villermaux [33]. In this context, the present approach provides a near-term solution to the complete 3-D nonlinear problem, and an advancement over the simpler linear-based theories that are currently the main recourse for analysts who must estimate droplet sizes. There is substantial use of this approach in the prior literature [34–36]. For example, Mehdizadeh *et al.* [36] confirms, analytically and experimentally, validation of the applicability of the Rayleigh–Taylor instability theory [37] (based on linear analysis) for predicting the number of 'fingers' around the ring edge. Mehdizadeh *et al.* found the fastest growing wave in the circumferential direction as a function of Weber number. Dombrowski and Johns [38] classic treatment of liquid sheets

contains a linear analysis of transverse instability for columns initially pinched from the parent surface.

3.1. Three-dimensional droplet tracking

The 2-D droplet tracking algorithm is expanded to 3-D to get a more realistic spray simulation. The velocity and the position for 3-D tracking are found by a co-ordinate transformation to the circumferential direction with the azimuthal location of a given drop being set randomly to get more a realistic image. That is, when we put droplets along the circumferential surface, the first position of the shed droplet is located randomly. If this practice is not followed, then many droplets can be aligned at the same azimuth with respect to the flow direction.

Figure 3 shows the Hoyt–Taylor jet evolution with 3-D droplet tracking. The jet shown in this figure has the statistical properties of $\mathrm{SMD}/d = 1/22.1$, N_D (total droplet number) $= 34\,000$, and θ_D (cone angle) $= 30.0^\circ$ for the Hoyt–Taylor jet. The spray is much more complex for the case of 3-D tracking since many droplets look like locating at the same position in a plane figure even though actually they are located separately in space. From this 3-D trajectory simulation of droplets shed from the jet core, we can see the dispersion that is formed by shed droplets in Figure 5, which provides the final jet shape and the trace of each droplet trajectory up to the final simulation time. The 3-D trajectory simulation and visualization show the physical process well from drop formation to dispersion and help us understand the atomization process of liquid jet.

3.2. Entire jet simulation

For the simulations conducted to date, the simulation for most of the cases was conducted up to $t^* = 5$ due to computational cost since the BEM calculation requires the solution of a large matrix system four times for each time step using the Runge–Kutta time integration scheme. Even though the LU decomposition method was parallelized and improved the computational speed greatly, other problems (i.e. the computation limitation about total memory, the networking speed, and the high dependency of computation time on total node number, etc.) prohibited longer simulations. To overcome this problem, the 'sponge' zone method which was presumed to absorb all disturbances with non-reflecting boundary condition was implemented through the previous work [30]. The 'sponge' zone method improved the computational time by stretching the grid spacing in the initial bulb of fluid downstream of the atomization zone that begins to form near the orifice exit.

Here we used the computational advantage of the SOR method introduced in the previous section to perform a longer simulation. Since the SOR scheme is faster than the LU method, larger problems can be solved. For example, SOR does not require the intermediate buffer matrix at the inversion step and alleviates the problem of memory limitations. Numerical tests show that the SOR method is working for simulations of more than $t^* = 5.0$, therefore longer simulations are possible even though the speed is slightly slower than the LU method. As a result, we successfully simulated the entire jet of Hoyt–Taylor's case up to $t^* = 9.0$.

Figure 4 shows the entire jet obtained from the SOR method with the convergence criteria of $\mathrm{Residue} = 1 \times 10^{-6}$ which is supposed to be appropriate since the prior numerical test did not show any meaningful discrepancy in statistical properties below this convergence criteria. The statistical properties of this whole jet simulation are summarized in Table I. There are no major differences in the statistical properties between Case (a) by LU and Case (b) by SOR

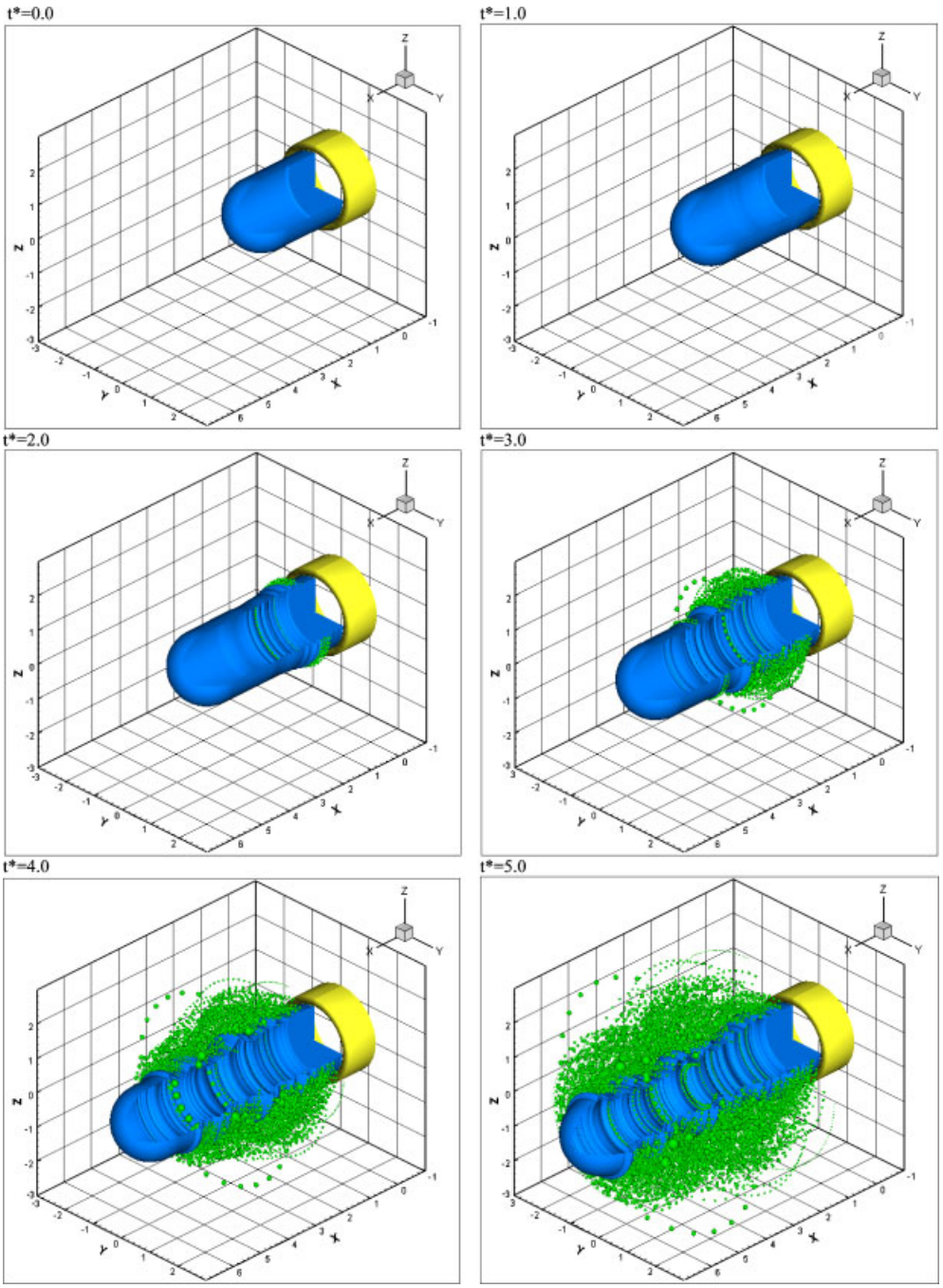

Figure 3. 3-D jet visualization for Hoyt–Taylor's jet.

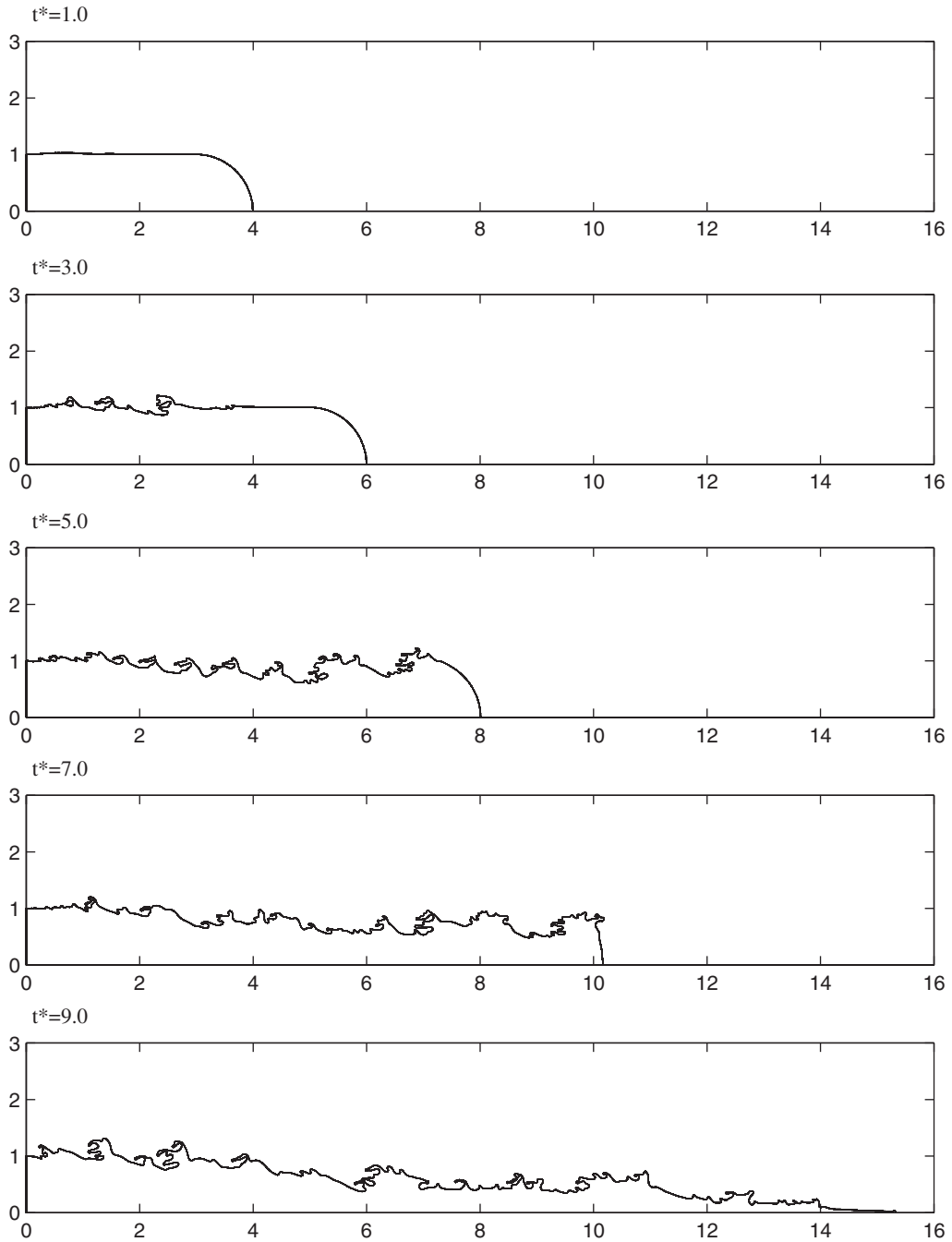

Figure 4. Liquid core simulation for Hoyt–Taylor's jet.

Table I. Statistical properties for an entire jet with simulation time.

	Case (a) for $t^* = 5.0$ by LU	Case (b) for $t^* = 5.0$ by SOR	Case (c) for $t^* = 9.0$ by SOR
Run time (CPU)	3.1 days (2 CPU)	3.2 days (1 CPU)	3.0 months (1CPU)
d/SMD	22.13	21.73	18.58
N_D	34 002	36 135	105 924
d/D_D	22.40	22.09	20.36
$\bar{u}_D/U$	0.801	0.796	0.877
$\bar{v}_D/U$	0.463	0.471	0.450
$\theta_D(^\circ)$	30.04	30.61	27.14
$\bar{N}_D$/ring	77.81	85.37	66.12
Stnd. dev.	60.61	87.70	59.73

up to $t^* = 5.0$. We confirm that the SOR is working well from this result. As shown at Case (C) of Table I, the simulation time increases rapidly as the jet length increases. It is a time-consuming problem and requires about 3 months of computational time on a LINUX-based system with a 2.2 GHz single processor. Actually, while the jet length is changed by a factor of two, the surface length must be changed by a larger ratio as shown in Figure 4. However the SMD, which stands for global flow atomization properties, is not changed greatly.

The complete simulation of Hoyt–Taylor's jet up to $t^* = 9.0$ is shown in Figure 4. The jet structure is initially assumed to be a simple cylinder with a hemispherical tip. When $t^* > 5.0$, the jet shape is quite interesting. As the jet grows, this hemispherical tip is deformed and absorbed to the jet core, which is not seen at the previous simulation for 5.0. The mean velocity of most droplets is in the stream-wise direction as a droplet moves along with the main jet stream. On the other hand, the velocity induced by the vortex penetrates to the jet surface and results in primary atomization. A more unstable surface then results in more vigorous pinch-off of the ligament from the jet core and therefore secondary atomization. The core length is the result of interaction between this mass loss and convective mean velocity of the main jet. From this BEM simulation, the jet core has a fairly large cone shape as seen at the last time plot in Figure 5. The whole length is about $L_{tot} = 15.0$ which is about two times that of the simulation for $t^* = 5.0$. This core length is substantially smaller than that observed from the experimental result due mainly to the excessive mass loss of axisymmetric simulation. However, droplet size comparisons have still been quite good [30].

The entire jet shape with 3-D droplet tracking is provided in Figure 5. Since no vaporization and no collisions are assumed, the droplet diameter is unchanged after the initial pinch-off event in these figures. The spray core angle evolves naturally as a part of the calculation. The cone angle tends to be over-predicted due to the fact that viscosity is neglected, the model is axisymmetric, droplet collisions are not simulated, and the aerodynamic interaction with an environmental gas is not included.

3.3. Secondary breakup and atomization after pinch-off

We have applied Ponstein's [24] linear stability theory of a vortex ring assuming an instantaneous secondary instability and Ponstein provided the dispersion equation of the vortex ring

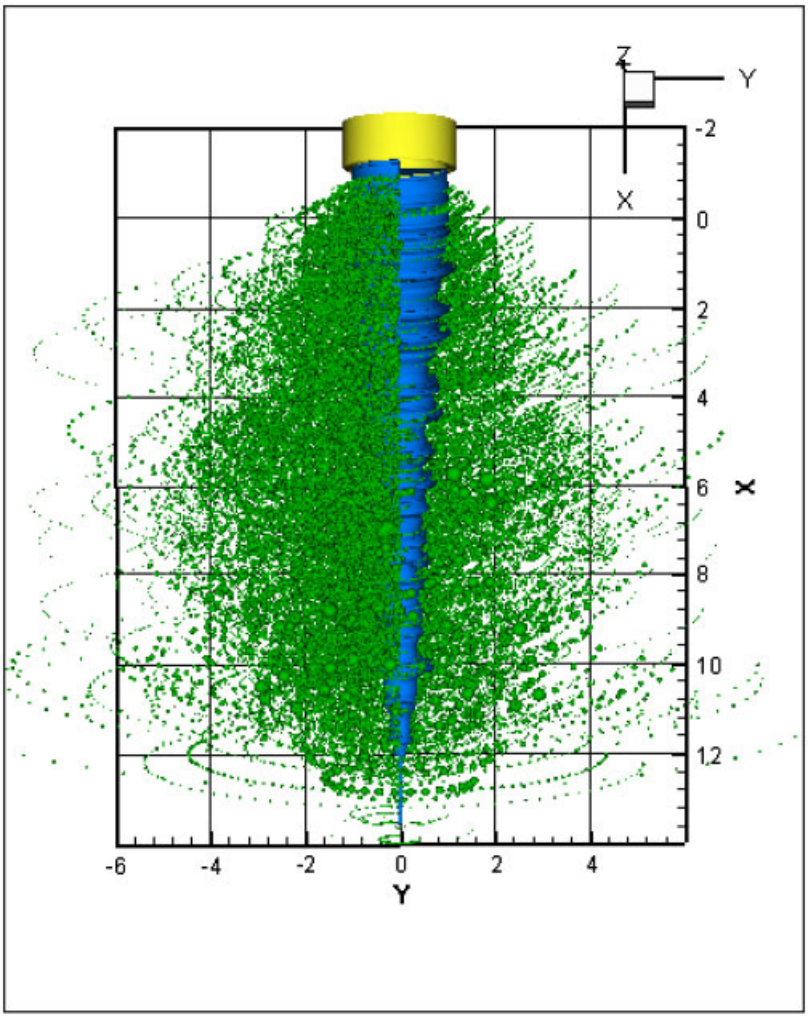

Figure 5. Entire jet visualization with 3-D droplet tracking for Hoyt–Taylor's jet.

as Equation (18). Wu *et al.* [16] provided both an empirical model and an experimental observation for the SMD of the initial primary breakup.

$$\frac{\mathrm{SMD}}{d} = \frac{77.5}{We_{l,d}^{0.74}} \tag{19}$$

The experiment was conducted for water with $d = 6.4$ mm, $U = 19$ and 22 m/s. These are close to the values, $d = 6.35$ mm and $U = 21$ m/s, used by Hoyt and Taylor. A relatively large difference between the predicted SMD and the experimental data at higher velocity range was reported.

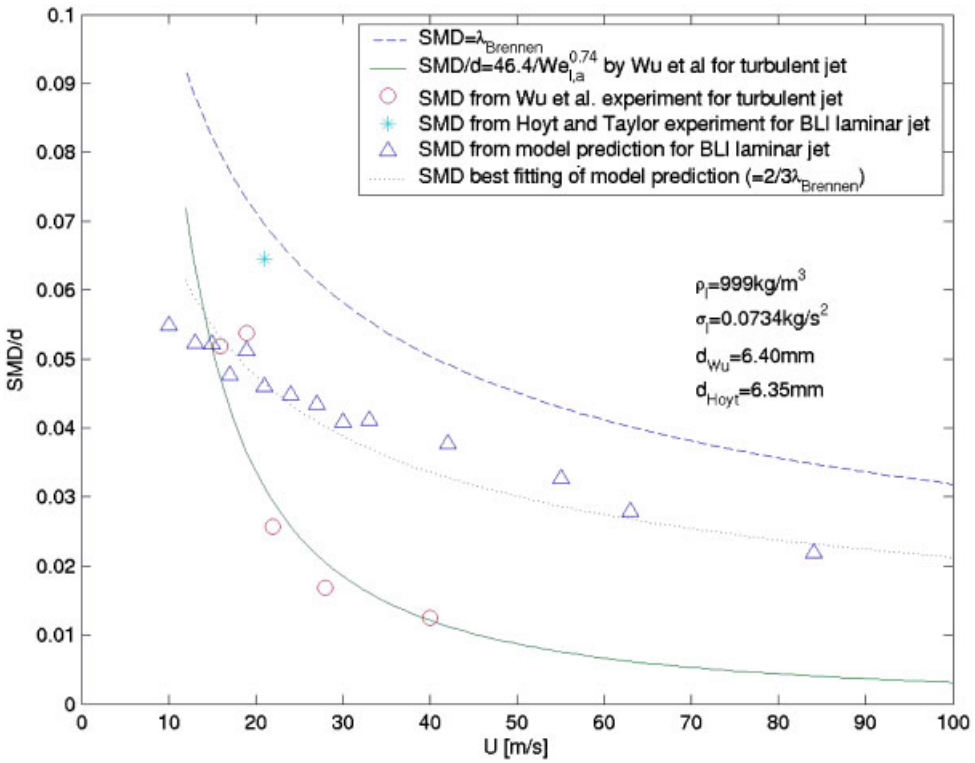

Figure 6. SMD comparison of predicted result based on BEM, Brennen's theory [28], and Wu *et al.*'s experimental result [16].

The current spray jet simulation based on BEM method shows good agreement with the Wu *et al.*'s experiment and the predicted results by Brennen's linear theory at jet speed near $U = 20$ m/s. However, it shows a greater discrepancy at higher jet velocity as shown in Figure 6. This discrepancy is attributed to a turbulence transition; or the role of turbulence becoming an important factor in this region. In later work [39], Faeth's group reports a transition to turbulence between 16 and 26 m/s; in the range where the dramatic changes in drop sizes occur. Turbulent eddies are interacting with the mean vorticity produced in the boundary layer to affect the wavelengths of instability and hence the drop sizes. References [8, 39] is suggested for further discussion on the transitional behaviour of the water jet.

Ligaments shed from the parent jet have been tracked in order to assess the potential for secondary breakup in the axisymmetric modes. A typical ligament formation process on the jet surface of the Hoyt–Taylor case is seen in Figure 7. This ligament is the 94th ligament obtained from the liquid jet simulation by the BEM and is shedding with a velocity of $U_r = 0.57U$ and direction of $\theta = 19.2°$ from the horizontal line at the time of $t^* = 3.18$. Figure 8 shows the motion and shape evolution subsequent to a pinching event. Here it is very interesting that the path obtained by BEM tracking is consistent with that of 2-D droplet

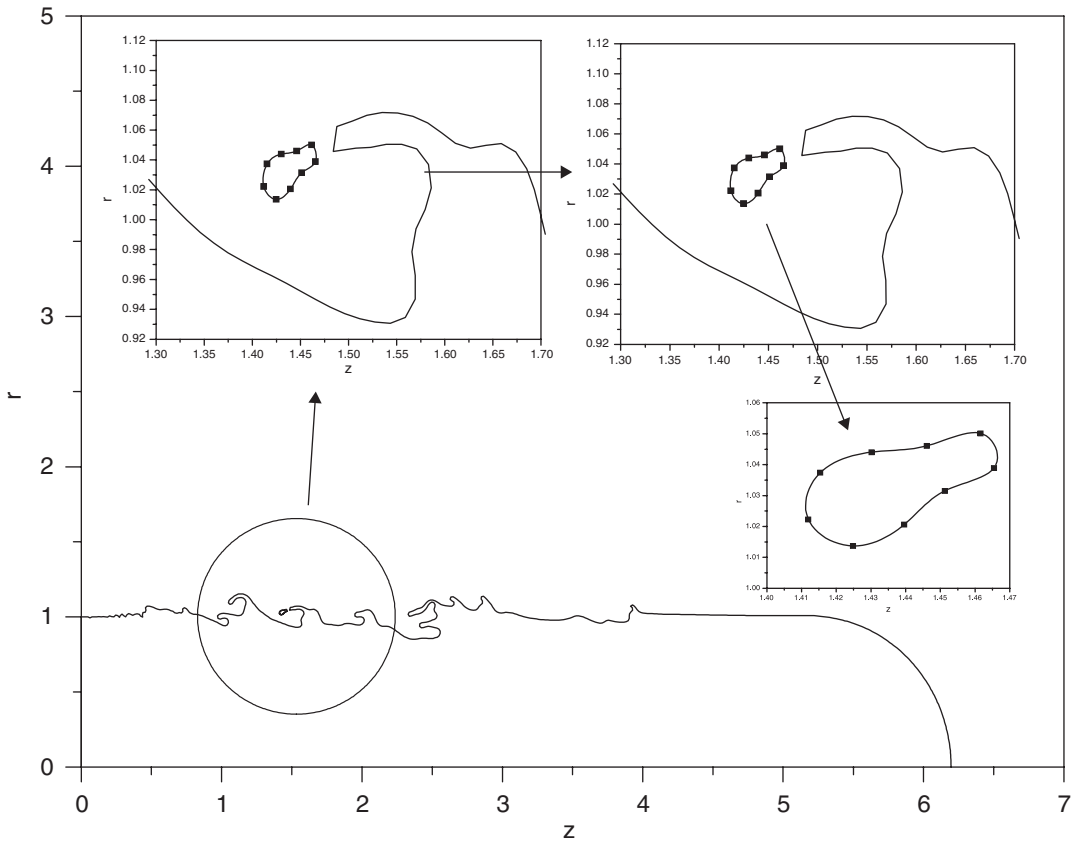

Figure 7. Typical ligament formation from parent of Hoyt and Taylor jet, captured at $t^* = 3.18$ s, 94th ligament.

tracking as a point mass. On the other hand, Figure 9 shows the ligament breakup process for a typical ligament shed from the parent jet, which is the typical case of secondary breakup obtained from several case studies. In this case, the ring fractionates into three smaller rings; an effect that would have significant repercussions on drop size predictions. Up to this investigation, a typical case for secondary breakup of shed ligaments was that a ligament breaks into three smaller ligaments including a satellite ligament during the computational time of $t^* = 5.0$. This breakup process including a satellite ligament is a very typical behaviour in the nonlinear region, which is investigated by prior researchers [32]. The initial kinetic energy is large enough to overcome surface tension.

Unfortunately, the analysis of the rings is a tedious process since hundreds are formed in a typical calculation. Therefore, only several cases have been studied for the conditions consistent with the Hoyt and Taylor experiment. It was found that every ligament which is formed from the parent jet breaks into smaller ligament. Even though the location of secondary instability depends on the initial condition such as shape and velocity distribution, the secondary breakup occurs within 0.1 orifice diameter in most cases. In addition, it has

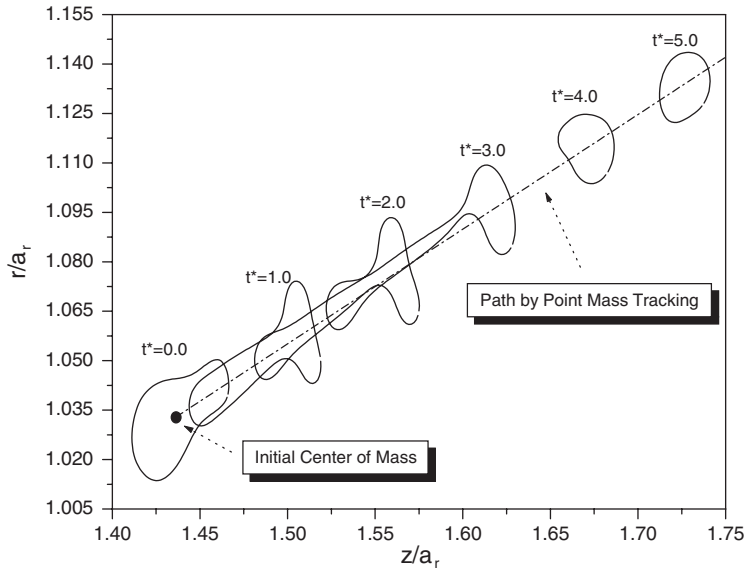

Figure 8. Typical secondary breakup process and path comparison between ligament breakup simulation using BEM and 2-D point mass tracking method.

to noted here that the time is non-dimensionalized by the characteristic value about rings as $t_r^* = U_r/a_r t_r$ in Equation (12), which means that the actual physical time given in these figures is much smaller than that expressed from the parent jet simulation. Since $U_r = 0.910\,U_j$ and $a_r = 1/10.5\,a_j$, the physical time should be scaled down by about a tenth, actually $\frac{1}{9.6}$, compared with that of parent jet simulation. The physical time of this ligament simulation has the order of tens of μs from this calculation. Thus, it is evident that the rings breakup very quickly as they are shed from the parent jet.

Results from various ligaments shed from the Hoyt–Taylor jet do show secondary breakups of the ligaments that would reduce effective SMD values. Consequently, it shows that applying Ponstein's theory to predict the droplet diameter, which does not account for the secondary breakup, could have substantial errors. Presumably, this secondary breakup must be strong at the higher speed jets because the velocity difference would be increased proportionally. This observation gives a possible explanation as to why the difference between the simulation result and experimental data is quite large at higher speeds in Figure 6. However, we have to note that the difference is too large to attribute entirely to this effect since our SMD result is approximately four times larger than experimental result for the higher jet speed regime. The difference in the role of the dominant instability mechanism is another possible reason for addressing the large difference in the droplet size between our boundary layer instability jet and the turbulent jet. As mentioned previously, the Ponstein theory tends to over-predict the droplet size because the nonlinear effect for the vortex-ring analysis is not taken into account [23], which amplifies the difference in SMD results since the SMD is predominantly affected by the larger droplet sizes (i.e. $\mathrm{SMD} \sim D^3/D^2$).

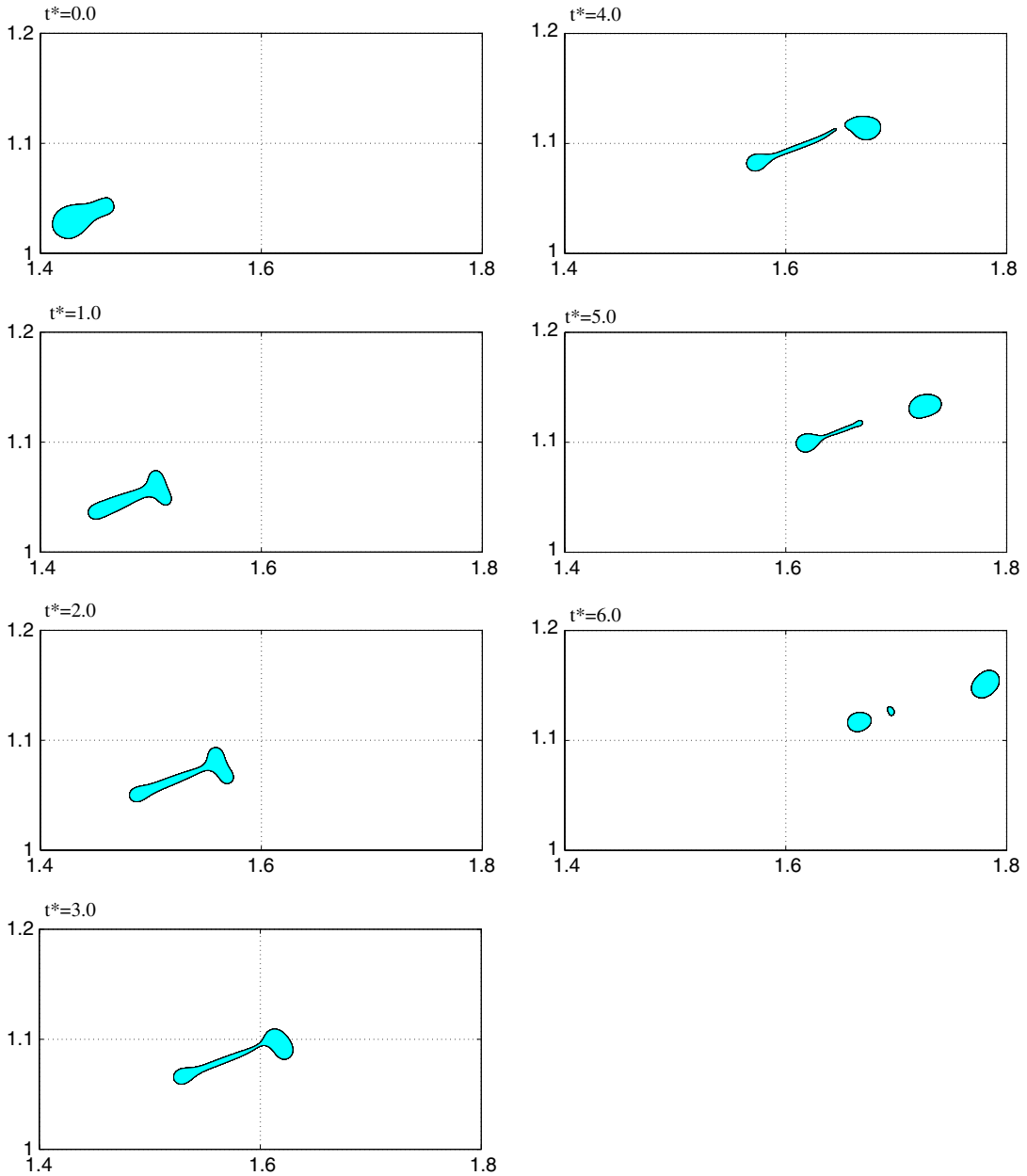

Figure 9. Typical secondary breakup process of pinch-off ligament, 94th ligament, $We = 1503$.

3.4. *Effect of Weber number to secondary breakup*

If the Weber number is decreased below a certain value, secondary breakup does not occur as shown in Figure 10. This simulation was done at the same initial condition as that of the

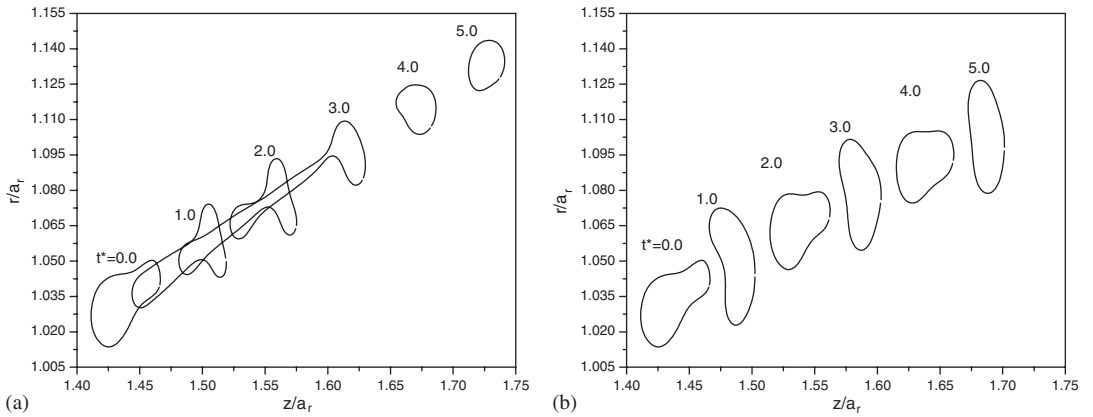

Figure 10. The effect of Weber number to secondary breakup: (a) when $We = W_{e0}(= 1503)$; and (b) when $We = W_{e0}/50(= 30)$.

94th ligament except the changed Weber number. The behaviour of the ligament is determined by the interaction between inertial forces and surface forces, since they are the only forces acting on it under the circumstance of inviscid, single-phase flow. That is, if the inertial force, which is represented by velocity, is larger than the surface tension, atomization will be occur. However, if the surface tension is sufficiently large enough to overcome the inertial force, the ring shows oscillatory motion without breakup as shown in Figure 10. Thus, there must be a critical Weber number which determines whether the breakup occurs or not. For this simulation, this critical Weber number is likely to be near that value corresponding to the five times larger surface tension ($We = 300$) because the ligament is not broken into smaller ligaments for this case. It is very interesting to note that the ligament shows almost perfectly oscillatory behaviour without breakup like a bouncing ball if the surface tension is increased by 50 times as shown in Figure 10.

3.5. Drop size distribution

One of the major advantages of the current model is the capability to predict droplet size distributions from a detailed nonlinear simulation. Figure 11 shows the cumulative drop size distribution for the Hoyt–Taylor jet simulation at the final simulation time. The estimated mass mean diameter (MMD) from this plot is $\mathrm{MMD}_{\mathrm{cal}}/d = 0.078$, which means that 50% of total liquid volume is in drops of smaller diameter. Therefore the ratio of mass median diameter (MMD) and SMD is

$$\left(\frac{\mathrm{MMD}/d}{\mathrm{SMD}/d}\right)_{\mathrm{cal}} = \frac{0.078}{0.054} = 1.44 \tag{20}$$

The Wu *et al.*'s experimental result [16] gives $(\mathrm{MMD}/\mathrm{SMD})_{\mathrm{exp}} = 1.2$, which obeys Simmon's [25] universal root normal distribution. Further investigation is needed to know what causes the difference in two predicted values. It is suspected that the Ponstein's theory cannot account for the smaller satellite droplet due to nonlinearity at secondary ligament breakup of peripheral direction because the theory is based on the linear analysis. Also, as it

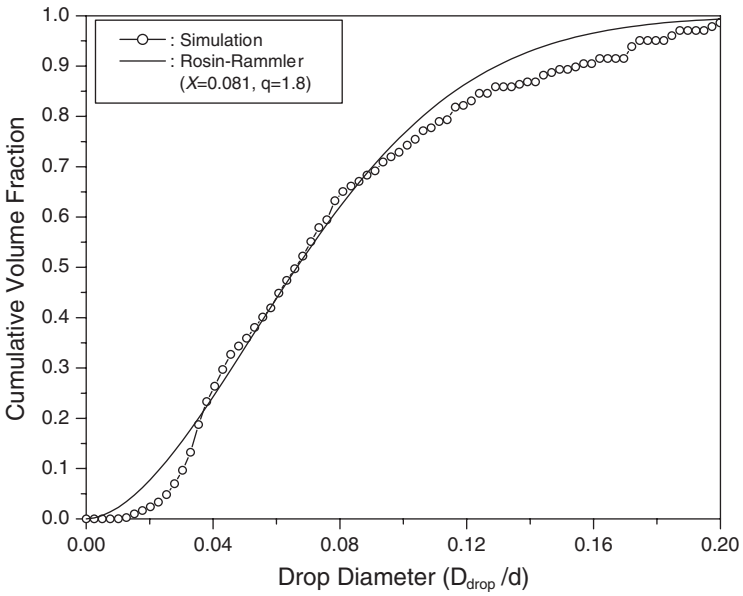

Figure 11. Cumulative volume fraction distribution for HT jet simulation.

was shown in the previous section for the secondary breakups of the ligaments, the secondary atomization while moving downstream would reduce the droplet size. As another reason, the SMD difference could result from aerodynamic effects; i.e. our primary atomization simulation does not account for aerodynamic force imposed by the gas.

The Rosin–Rammler (RR) model is frequently employed to describe the cumulative volume distribution:

$$\mathrm{CDF} = 1 - \exp\{-(D/X)^q\} \tag{21}$$

where cumulative density function (CDF) is the fraction of the total volume contained in drops of diameter less than D. The characteristic droplet size, X, can be expressed as $X = D_{10}/\Gamma(1/q + 1)$ [40], where D_{10} is the arithmetic mean diameter. Γ is the gamma function, and q, so-called, 'dispersion coefficient', indicates the width of the distribution. Small value of q indicates broad distribution and large value of q means narrow distribution. The comparison between the Rosin–Rammler distribution and our simulation result is given in Figure 11. As shown in this figure, they are well matched at the values of $X = 0.081$ (note, that X is non-dimensionalized by the orifice diameter, d) and $q = 1.8$. Since the corresponding q value is relatively small, the drop size is supposed to be distributed widely in our simulation result. Further studies are necessary to assess the viability of the model in predicting actual droplet size distributions for sprays. Unfortunately, the high jet velocities associated with true sprays pose challenging conditions for computations in the current computing environment. However, it is noteworthy that Yoon *et al.* [40] too found that the Rosin–Rammler distribution function is an appropriate model for describing the droplet distribution near the nozzle exit (or near the liquid core). Moreover, Yoon *et al.* indicate that the dispersion coefficient, q, is normally less than $q < 2.0$ at the nozzle exit because the liquid core produces the droplet sizes of a

wide range. Our finding of this report is, therefore, consistent with the observation of Yoon *et al.* [40].

4. CONCLUSIONS

A fully nonlinear model has been developed to assess the time-dependent evolution of an axisymmetric axial liquid jet using a boundary element method. By using this developed BEM model, substantial efforts have been made so far in assessing the instability and unsteady atomization processes in liquid jets.

The current spray jet simulation based on BEM method shows a good agreement with experimental results and the results measured by Hoyt and Taylor in their classic experiment [9]. However, greater differences are seen for higher velocity jets with the model significantly overpredicts droplet sizes. It has been shown that the secondary breakups of the ring-shaped ligaments can account for some of the differences. It was found that virtually every ligament which is formed from the Hoyt and Taylor parent jet breaks into smaller ligaments. Even though the location of secondary instability depends on the initial condition and shape, the secondary breakup occurs within 0.1 orifice diameters in most cases. The investigation of various ligaments shed from jet core shows secondary breakups of the ligaments that would reduce effective SMD values; it could make its render results much closer to Wu *et al.*'s [16] result.

The 3-D droplet tracking algorithms have been developed to account for aerodynamic drag subsequent to ring formation. The trajectory of droplet tracking as a point mass was well matched with the moving path obtained by BEM simulation for each droplet. By adding a trajectory simulation of droplets shed from jet core, we can see the dispersion of droplets that is formed by shed droplets more clearly. The 3-D trajectory simulation for each droplet shows the physical process well from drop formation to dispersion, and helps understanding of the atomization process in a liquid jet and the formation of the spray cone.

Using the linear stability analysis of Ponstein in concert with the ligament conditions permits the development of droplet size distributions from first principals. The distributions found for the Hoyt and Taylor's jet show a wide range of droplet sizes and can be matched using the popular Rosin–Rammler model.

NOMENCLATURE

U	jet speed
z	axial direction
r	radial direction
s	distance along the surface
u	axial velocity
v	radial velocity
θ	direction of velocity from vertical line
a	nozzle radius
a_{r}	droplet radius
δ_2	momentum thickness
ρ	density

σ	liquid surface tension
ϕ	velocity potential
β	surface slope
κ	surface curvature
λ	most dominant wavelength
Γ	circulation
γ	non-dimensional frequency
N_{D}	number of droplets
Bo	Bond number
We	Weber number
q	velocity normal to jet surface, Rossin–Rammler parameter (Equation (21))
BLI	boundary layer instability
MMD	mass median diameter
SMD	Sauter mean diameter

Subscripts

a	nozzle radius, a, is used for length dimension (i.e. $We_{a,\mathrm{l}} = \rho_{\mathrm{l}} U^2 a/\sigma$)
D	droplet property
g	gas property
l	liquid property
t	total or general solution
v	filament vortex ring located at nozzle exit

Superscript

$*$	non-dimensional parameter

ACKNOWLEDGEMENTS

The authors greatly acknowledge the support of the Airforce Office of Scientific Research (Grant number F49620-03-1-0025) with programme manager Dr Mitat Birkan. The second author acknowledges the support received from Sandia National Laboratories, which is a multiprogram laboratory operated by Sandia Corporation, a Lockheed Martin Company for the United States Department of Energy's National Nuclear Security Administration under contract DE-AC04-94AL85000.

REFERENCES

1. Rupe JH. On the dynamic characteristics of free liquid jets and a partial correlation with orifice geometry. *NASA JPL Technical Report*, *32-207*, 1962.
2. Hiroyasu H, Arai M, Shimizu M. Break-up length of a liquid jet and internal flow in a nozzle. *CLASS-91*, 1991; 275–282.
3. Karasawa T, Abe K, Shiga S, Kurabayashi T. Effect of nozzle configuration on the atomization of a steady spray. *Atomization and Sprays* 1992; **2**:411–426.
4. Tamaki N, Nishida K, Hiroyasu H, Shimizu M. Effect of cavitation and internal flow on atomization of a liquid jet. *Atomization and Sprays* 1998; **8**:179–197.
5. McCathy MJ, Molloy MA. Review of stability of liquid jets and influence of nozzle design. *The Chemical Engineering Journal* 1974; **7**:1–20.
6. Xu C, Bunnell RA, Heister SD. On the influence of internal flow structure on performance of plain-orifice atomizers. *Atomization and Sprays* 2001; **11**:335–349.

7. Shkadov VY. Wave formation on surface of viscous liquid due to tangential stress. *Fluid Dynamics* 1970; **5**:473–476.
8. Yoon SS, Heister SD. A nonlinear atomization model based on a boundary layer instability mechanism. *Physics of Fluids* 2004; **16**:47–61.
9. Hoyt JW, Taylor JJ. Waves on water jets. *Journal of Fluid Mechanics* 1977; **83**:119–127.
10. Bergwerk W. Flow pattern in diesel nozzle sprays holes. *Proceedings of the Institution of Mechanical Engineers* 1959; **173**:655–660.
11. Chaves H, Knapp M, Kubitzek A. Experimental study of cavitation in the nozzle hole of diesel injectors using transparent nozzles. *SAE*, *No. 950290*, 1995.
12. Nurick WH. Orifice cavitation and its effect on spray mixing. *Journal of Fluids Engineering* 1976; **98**: 681–687.
13. Bunnell RA, Heister SD. Three-dimensional unsteady simulation of cavitating flows in injector passages. *Journal of Fluids Engineering* 2000; **122**:791–797.
14. Soteriou C, Andrews R, Torres N, Smith M, Kunkulagunta R. Through the diesel nozzle hole—a journey of discovery. *ICLASS-2001 Conference Proceedings*, Dearborn, MI, 2001.
15. Hoyt JW, Taylor JJ. Turbulence structure in a water jet discharging in air. *Physics of Fluids* 1977; **20**(10): s253–s257.
16. Wu PK, Tseng LK, Faeth GM. Primary breakup in gas/liquid mixing layers for turbulent liquids. *Atomization and Sprays* 1992; **2**:295–317.
17. Wu PK, Faeth GM. Aerodynamic effects on primary breakup of turbulent liquids. *Atomization and Sprays* 1993; **3**:265–289.
18. Tseng LK, Ruff GA, Faeth GM. Effects of gas density on the structure of liquid jets in still gases. *AIAA Journal* 1992; **30**:1537–1544.
19. Reitz RD, Bracco FV. Mechanism of atomization of a liquid jet. *Physics of Fluids* 1982; **25**(10):1730–1742.
20. Lin SP, Lian ZW. Mechanics of breakup of liquid jets. *AIAA Journal* 1990; **28**:120–126.
21. Lin SP, Webb R. Nonaxisymmetric evanescent waves in a viscous liquid jet. *Physics of Fluids* 1994; **6**:2545–2547.
22. Sterling AM, Sleicher CA. The instability of capillary jets. *Journal of Fluid Mechanics* 1975; **68**:477–495.
23. Yoon SS, Heister SD. Categorizing linear theories for atomizing round jets. *Atomization and Sprays* 2003; **13**:499–516.
24. Ponstein J. Instability of rotating cylindrical jets. *Applied Scientific Research* 1959; **8**(6):425–456.
25. Simmons HC. The correlation of drop-size distributions in fuel nozzle sprays. *Journal of Engineering for Power* 1977; **99**:309–319.
26. Liggett JA, Liu PL. *The Boundary Integral Equation Method for Porous Media Flow*. George Allen and Unwin: London, 1983.
27. Yoon SS, Heister SD. Analytical formulas for the velocity field induced by an infinitely thin vortex ring. *International Journal for Numerical Methods in Fluids* 2004; **44**:665–672.
28. Brennen C. Cavity surface wave patterns and general appearance. *Journal of Fluid Mechanics* 1970; **44**(1):33–49.
29. White FM. *Viscous Fluid Flow* (2nd edn). McGraw-Hill: New York, 1991; 235, 269, 358.
30. Yoon SS, Heister SD. A fully nonlinear model for atomization of high-speed jets. *Engineering Analysis with Boundary Elements* 2004; **28**:345–357.
31. Hwang S, Liu Z, Reitz RD. Breakup mechanisms and drag coefficients of high speed vaporizing liquid drops. *Atomization and Sprays* 1996; **6**:353–376.
32. Hilbing JH, Heister SD, Spangler CA. A boundary-element method for atomization of a finite liquid jet. *Atomization and Sprays* 1995; **5**:621–638.
33. Marmottant P, Villermaux E. On spray formation. *Journal of Fluid Mechanics* 2004; **498**:73–111.
34. Kim HY, Feng ZC, Chun JH. Instability of a liquid jet emerging from a droplet upon collision with a solid surface. *Physics of Fluids* 2000; **12**:531–541.
35. Aziz SD, Chandra S. Impact, recoil and splashing of molten metal droplets. *International Journal of Heat and Mass Transfer* 2000; **43**:2841–2857.
36. Mehdizadeh NZ, Chandra S, Mostaghimi J. Formation of fingers around the edges of a drop hitting a metal plate with high velocity. *Journal of Fluid Mechanics* 2004; **510**:353–373.
37. Allen RF. The role of surface tension in splashing. *Journal of Colloid and Interface Science* 1975; **51**:350–351.
38. Dombrowski N, Johns WR. The aerodynamic instability and disintegration of viscous liquid sheets. *Chemical Engineering Science* 1963; **18**:203–214.
39. Wu PK, Miranda RF, Faeth GM. Effects of initial flow conditions on primary breakup of nonturbulent and turbulent liquid jets. *32th Aerospace Sciences Meeting and Exhibit*, *AIAA 94-0561*, Reno, NV, 1994.
40. Yoon SS, Hewson JC, DesJardin PE, Glaze DJ, Black AR, Skaggs RR. Numerical modeling and experimental measurements of a high speed solid-cone water spray for use in fire suppression applications. *International Journal of Multiphase Flows* 2004; **30**:1369–1388.

